Atmos. Chem. Phys., 20, 13417–13424, 2020
https://doi.org/10.5194/acp-20-13417-2020

Atmospheric Chemistry and Physics
Open Access

Technical Note: Effect of varying the λ = 185 and 254 nm photon flux ratio on radical generation in oxidation flow reactors

Jake P. Rowe[1,a,★], **Andrew T. Lambe**[2,★], **and William H. Brune**[1]

[1]Department of Meteorology and Atmospheric Science, Pennsylvania State University, University Park, PA, USA
[2]Center for Aerosol and Cloud Chemistry, Aerodyne Research Inc., Billerica, MA, USA
[a]now at: Department of Chemistry, University of Colorado, Boulder, CO, USA
★These authors contributed equally to this work.

Correspondence: Andrew T. Lambe (lambe@aerodyne.com)

Received: 26 June 2020 – Discussion started: 7 July 2020
Revised: 29 September 2020 – Accepted: 5 October 2020 – Published: 12 November 2020

Abstract. Oxidation flow reactors (OFRs) complement environmental smog chambers as a portable, low-cost technique for exposing atmospheric compounds to oxidants such as ozone (O_3), nitrate (NO_3) radicals, and hydroxyl (OH) radicals. OH is most commonly generated in OFRs via photolysis of externally added O_3 at $\lambda = 254$ nm (OFR254) or combined photolysis of O_2 and H_2O at $\lambda = 185$ nm plus photolysis of O_3 at $\lambda = 254$ nm (OFR185) using low-pressure mercury (Hg) lamps. Whereas OFR254 radical generation is influenced by [O_3], [H_2O], and photon flux at $\lambda = 254$ nm (I_{254}), OFR185 radical generation is influenced by [O_2], [H_2O], I_{185}, and I_{254}. Because the ratio of photon fluxes, $I_{185} : I_{254}$, is OFR-specific, OFR185 performance varies between different systems even when constant [H_2O] and I_{254} are maintained. Thus, calibrations and models developed for one OFR185 system may not be applicable to another. To investigate these issues, we conducted a series of experiments in which $I_{185} : I_{254}$ emitted by Hg lamps installed in an OFR was systematically varied by fusing multiple segments of lamp quartz together that either transmitted or blocked $\lambda = 185$ nm radiation. Integrated OH exposure (OH_{exp}) values achieved for each lamp type were obtained using the tracer decay method as a function of UV intensity, humidity, residence time, and external OH reactivity (OHR_{ext}). Following previous related studies, a photochemical box model was used to develop a generalized OH_{exp} estimation equation as a function of [H_2O], [O_3], and OHR_{ext} that is applicable for $I_{185} : I_{254} \approx 0.001$ to 0.1.

1 Introduction

Hydroxyl (OH) radicals govern the concentrations of most atmospheric organic compounds, including those that lead to secondary organic aerosol (SOA) formation. For decades, environmental chambers and oxidation flow reactors (OFRs) have been used to simulate atmospheric aging processes through the controlled exposure of trace gases and aerosols to OH radicals. Environmental chamber studies are typically conducted over experimental timescales and equivalent atmospheric exposure times of hours up to 1 or 2 d. OFRs with residence times on the order of minutes achieve multiple days of equivalent atmospheric OH exposure (OH_{exp}), typically through the following reactions:

$$O_3 + h\nu_{254} \rightarrow O_2 + O(^1D) \quad \text{(R1)}$$

$$O(^1D) + H_2O \rightarrow 2OH \quad \text{(R2)}$$

$$O(^1D) + N_2O \rightarrow 2NO. \quad \text{(R3)}$$

This method is referred to as OFR254 and relies on addition of externally generated O_3 at the OFR inlet. In some cases, OFRs have additionally employed the secondary $\lambda = 185$ nm emission line present in low-pressure mercury (Hg) lamps to generate radicals from the following reactions in addition to those listed above that are employed in OFR254:

$$H_2O + h\nu_{185} \rightarrow H + OH \quad \text{(R4)}$$

$$H + O_2 \rightarrow HO_2 \quad \text{(R5)}$$

$$O_2 + h\nu_{185} \rightarrow 2O(^3P) \quad \text{(R6)}$$

$$O(^3P) + O_2 \rightarrow O_3 \quad \text{(R7)}$$

$$N_2O + h\nu_{185} \rightarrow N_2 + O(^1D). \quad \text{(R8)}$$

This method is referred to as OFR185. Recent modeling studies suggest that OFR185 is less affected by experimental artifacts than OFR254 such as SOA photolysis and unwanted reactions with non-OH oxidants (Peng et al., 2016, 2018, 2019). Additionally, OFR185 is often more practical than OFR254 for application in field studies because O_2 and H_2O that are already present in ambient air are photolyzed to generate O_3, OH, and HO_2, whereas OFR254 requires addition of compressed air or O_2 for external O_3 generation and additional inlet plumbing to inject it at the OFR inlet. However, because the $\lambda = 185$ nm photon flux (I_{185}) is influenced by OFR-specific design considerations that are mainly related to the Hg lamps being used, concentrations of O_3, $HO_x = OH + HO_2$, and $NO_x = NO + NO_2$ generated using OFR185 are potentially variable between different systems even when constant [H_2O], [N_2O], and I_{254} are established. Thus, calibrations and models developed for one OFR185 system may not be applicable to another, making it more difficult to evaluate results or plan experiments. To investigate these issues, we designed a series of experiments in which $I_{185} : I_{254}$ was systematically varied over a wide range using multiple novel Hg lamp configurations. Integrated OH_{exp} values were obtained as a function of OFR185 conditions, and a photochemical box model was used to develop a system of OH_{exp} estimation equations that are applicable to OFR185 systems with $I_{185} : I_{254} \approx 0.001$ to 0.1.

2 Experimental

Experiments were conducted using an Aerodyne Potential Aerosol Mass (PAM) OFR, which is a horizontal aluminum cylindrical chamber (46 cm long × 22 cm ID) operated in continuous flow mode (Lambe et al., 2011). A simplified schematic is shown in Fig. S1 in the Supplement. The H_2O mixing ratio in the OFR was controlled by passing the carrier gas through a Nafion humidifier (Perma Pure LLC) or heated recirculating water bath (Neslab Instruments, Inc.) and then diluting with different levels of dry carrier gas at the OFR inlet. A photodetector (TOCON-C6, sglux GmbH) and a relative humidity and temperature (RH/T) sensor (SHT21, Sensiron) were mounted in the exit flange of the OFR. Across all experiments, [H_2O] ranged from 0.03 % (1 % RH at 25.3 °C) to 3.9 % (88 % RH at 30.9 °C). The O_3 mixing ratio at the exit of the OFR was measured with a UV ozone analyzer (106-M, 2B Technologies).

2.1 HO_x generation

HO_x was produced via Reactions (R1)–(R2) and (R4)–(R7). Photolysis of H_2O, O_2, and O_3 in the OFR was achieved using two low-pressure Hg fluorescent lamps (Light Sources, Inc.) that were isolated from the sample flow using type 214 quartz sleeves. Nitrogen purge gas was flowed over the lamps to prevent O_3 buildup between the lamps and sleeves. A fluorescent dimming ballast was used to regulate current applied to the lamps. The dimming voltage applied to the ballast ranged from 0.8 to 10 V direct current (DC). Below ∼ 0.8 V DC, the lamp output was unstable due to flickering, and 10 V DC was the maximum control voltage permitted by the ballast.

Figure 1 shows the Hg fluorescent lamp configurations that were used in this study. Lamp type A is an ozone-producing low-pressure Hg germicidal fluorescent lamp (GPH436T5VH/4P, Light Sources Inc.) in which type 214 quartz that transmits $\lambda = 185$ and 254 nm radiation is present along the entire 356 mm arc length. This lamp type is a standard component of the Aerodyne PAM OFR. The relative transmissivity of $\lambda = 185$ nm radiation (T_{185}) in lamp type A is thus equal to 1. Lamp type B is equivalent to lamp type A with added segments of opaque heat shrink tubing applied to approximately 86 % of the arc length ($T_{185} \approx 0.14$; see also Fig. S2 in the Supplement) to reduce I_{185} and I_{254} to levels below what is achievable using the ballast dimming voltage. A different type of quartz is available (type 219) that blocks $\lambda = 185$ nm and transmits $\lambda = 254$ nm radiation ($T_{185} = 0$). To cover the largest possible range of $I_{185} : I_{254}$, lamp types C, D, and E (GPH436T5L/VH/4P 90/10, GPH436T5L/VH/4P 96/4, and GPH436T5L/VH/4P 98.5/1.5; Light Sources, Inc.) fused one segment each of quartz with $T_{185} = 0$ and $T_{185} = 1$ to provide reduced I_{185} relative to lamp type A while maintaining constant I_{254}. Finally, to evaluate the effect of lamp design at fixed T_{185} and I_{254}, lamp types F and G contain the same ratios of $T_{185} = 0$ and $T_{185} = 1$ quartz as types C and D, but with 5 and 13 total segments instead of 2 segments. These different designs isolate the effect of discretized $\lambda = 185$ nm irradiation across the entire arc length of the lamp vs. having all $\lambda = 185$ nm radiation near the entrance of the OFR.

2.2 OH_{exp} characterization studies

OH_{exp}, defined here as the product of the average OH concentration and the mean OFR residence time (τ_{OFR}), was characterized by measuring the decay of carbon monoxide (CO) and/or sulfur dioxide (SO_2) tracers using Thermo 48i and 43i CO and SO_2 analyzers (e.g., Lambe et al., 2011). Tracer mixing ratios entering the reactor were 6–9 ppmv for CO and 288–629 ppbv for SO_2, each diluted from separate gas mixtures of 0.5 % CO or SO_2 in N_2 (Praxair). The corresponding total external OH reactivity (OHR_{ext}), which is the summed product of each tracer mixing ratio and its bimolecular OH rate coefficient, ranged from approximately 9 to 64 s^{-1}. Tracer concentrations were allowed to stabilize before initiating OH_{exp} measurements, during which steady-state levels of CO and/or SO_2 were obtained with the lamps turned off. Then, the lamps were turned on, and tracer concentrations were allowed to equilibrate before being measured at illuminated steady-state conditions.

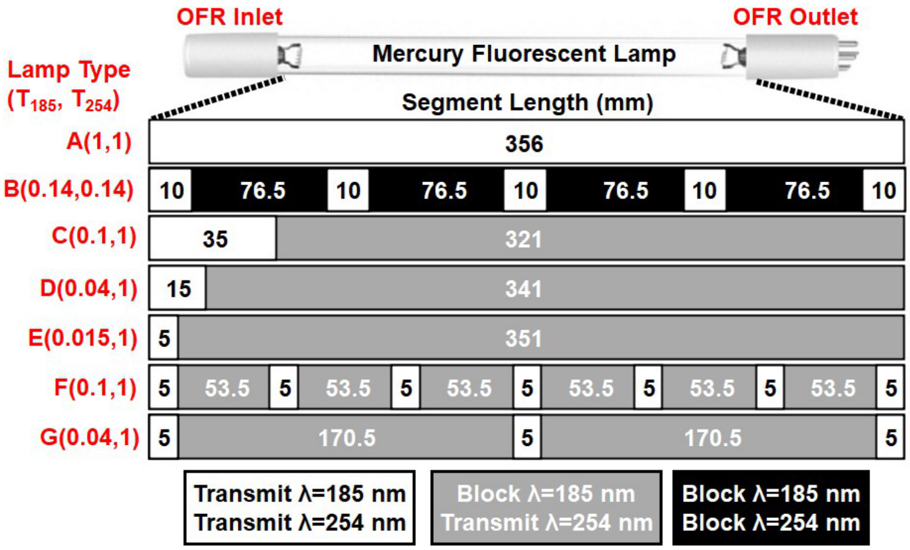

Figure 1. Low-pressure Hg fluorescent lamp types used in this study. Each lamp type contains 356 mm of quartz material that either transmits both λ = 185 and 254 nm radiation (white, $T_{185} = 1$), blocks λ = 185 nm and transmits λ = 254 nm radiation (grey, $T_{185} = 0$), or blocks both λ = 185 and 254 nm radiation (black, $T_{185} = 0$).

In most experiments, the calculated mean residence time was $\tau_{OFR} = 124$ s, which was obtained from the ratio of the internal OFR volume (≈ 13 L) and the total sample and makeup flow rate through the OFR (6.4 L min^{-1}). This calculation implicitly assumes plug flow conditions, with associated uncertainty of approximately 10 % compared to an explicit residence time distribution measurement at a specific OFR condition (Li et al., 2015). Variability in OFR parameters (e.g., temperature, flow rate) may increase the uncertainty in this assumption across a continuum of conditions (Huang et al., 2017; Lambe et al., 2019). To characterize the uncertainty in our plug flow approximation across multiple sample flow conditions, we measured integrated OH exposure (OH_{exp}) values of 3.3×10^{11}, 7.8×10^{11}, and 2.0×10^{12} molec. cm^{-3} s at sample flow rates of 12.5, 6.4, and 3.1 L min^{-1}, respectively, using the tracer decay method (Sect. 2.2) with the OFR operated at the same humidity and lamp intensity. Thus, perturbing the "plug flow" $\tau_{OFR} = 124$ s by a factor of 2 in either direction changed OH_{exp} by factors of 2.36 and 2.56. Based on these results, an upper-limit estimated uncertainty in τ_{OFR} and corresponding OH_{exp} is approximately 30 %.

2.3 Photochemical model

We used a photochemical model implemented in MATLAB and Igor Pro to calculate concentrations of radical/oxidant species produced in the reactor (Li et al., 2015). The KinSim chemical kinetic solver was used to compile the version of the model that was implemented in Igor Pro (Peng and Jimenez, 2019). Model input parameters are shown in Table 1, and reactions and associated kinetic rate coefficients that were included in the model are summarized in Table S1 in the Supplement (Peng and Jimenez, 2020a). For cases where $[H_2O] \leq 0.1$ % and the RH sensor accuracy became a limiting factor, we systematically adjusted the $[H_2O]$ value that was input to the model to a value between 0.01 % and 0.1 % to achieve better agreement between measured and modeled OH_{exp}. I_{254} and I_{185} values input to the model were adjusted to match the measured OH_{exp} values as best as possible within the following constraints:

Table 1. OFR conditions input to photochemical model.

P (mbar)	1013
T (°C)	22.5–31.9
Residence time (s)	63, 124, 251
H_2O (%)	0.03–3.9
O_3 (ppmv)	0.4–156
CO (ppmv)	0 or 6–9
SO_2 (ppbv)	0 or 288–629
I_{185} (photons cm^{-2} s^{-1})	1.1×10^{12}–3.2×10^{14}
I_{254} (photons cm^{-2} s^{-1})	6.0×10^{13}–4.2×10^{15}

1. $I_{254,max} = (3.5 \pm 0.7) \times 10^{15}$ photons cm^{-2} s^{-1} for two lamps operated at maximum output (Lambe et al., 2019).

2. At reduced lamp output, I_{254} was calculated by multiplying $I_{254,max}$ by the ratio of photodetector-measured irradiance values measured at maximum and reduced lamp output at λ = 254 nm.

3. $I_{185,max} : I_{254,max} \lessapprox 0.10$ for lamp types A and B only (Spicer, 2013).

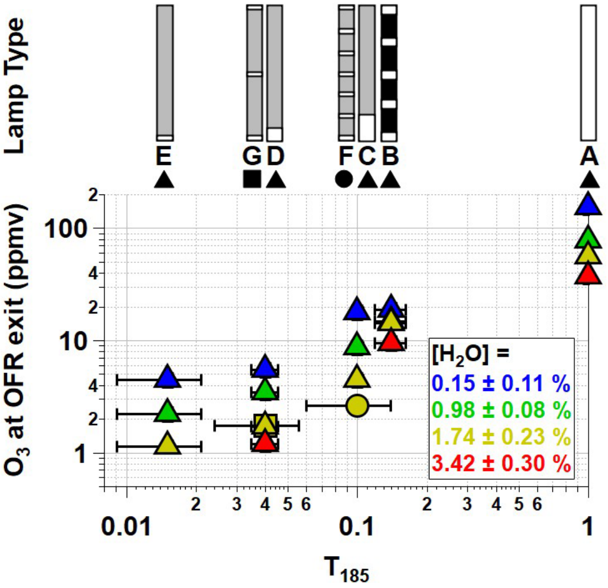

Figure 2. O_3 mixing ratio generated using OFR185 at $I_{254} = (3.5 \pm 0.7) \times 10^{15}$ photons cm^{-2} s^{-1} (lamp types A and C–G) and $I_{254} = 5.8 \times 10^{14}$ photons cm^{-2} s^{-1} (lamp type B) as a function of T_{185} and [H_2O]. Error bars represent $\pm 1\sigma$ of replicate O_3 measurements and ±2 mm uncertainty in lengths of individual $T_{185} = 0$ and 1 segments.

4. $I_{185,\mathrm{max}} : I_{254,\mathrm{max}} \lessapprox 0.01$, 0.004, and 0.0015 for lamp types C and F, D and G, and E, respectively.

5. At reduced lamp output, I_{185} was calculated by multiplying $I_{185,\mathrm{max}}$ by the ratio of O_3 mixing ratios measured at maximum and reduced lamp output.

Within these constraints, the mean ($\pm 1\sigma$) ratios of modeled to measured CO and SO_2 concentrations remaining at the exit of the OFR were 1.02 ± 0.06 and 0.97 ± 0.17, respectively.

3 Results and discussion

3.1 Influence of I_{185} on [O_3] and OH_{exp}

Figure 2 shows [O_3] measured at the exit of the OFR as a function of T_{185} with each lamp type operated at maximum UV output. Binned data are shown for conditions where [H_2O] = 0.15 % ± 0.11 %, 0.98 % ± 0.08 %, 1.74 % ± 0.23 %, and 3.42 % ± 0.30 %. At fixed [H_2O], [O_3] increased as a function of T_{185}. For example, [O_3] increased from 17.8 to 155 ppmv at [H_2O] = 0.15 % and from 4.5 to 56 ppmv at [H_2O] = 1.74 % as T_{185} increased from 0.1 to 1. At fixed T_{185} and I_{254}, [O_3] decreased with increasing [H_2O] due to faster $O(^1D) + H_2O$ reaction rate following O_3 photolysis at $\lambda = 254$ nm. Consequently, as [H_2O] increased from 0.15 % to 3.42 %, [O_3] decreased by a factor of 4–5 for lamp types A and C–G, whereas [O_3] decreased by a factor of 2 for lamp type B because of its reduced I_{254} (Fig. 1).

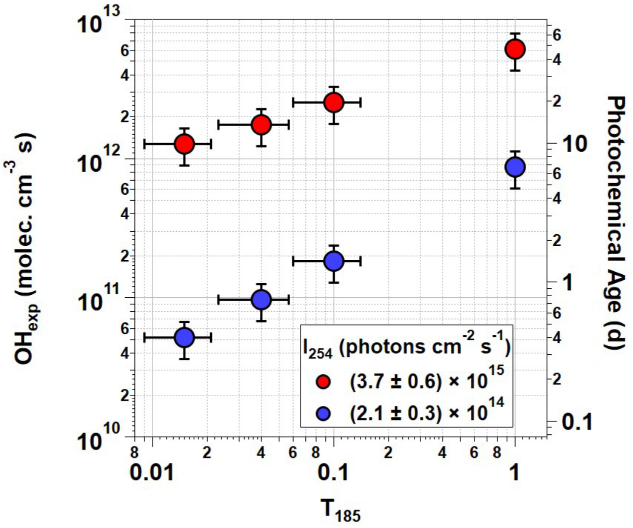

Figure 3. OH_{exp} generated using OFR185 ([H_2O] = 1.90 % ± 0.26 %) at minimum and maximum I_{254} for each T_{185} value. Corresponding photochemical age is shown on the right y axis assuming mean [OH] = 1.5×10^6 molec cm^{-3} (Mao et al., 2009). Error bars assume ±30 % uncertainty in OH_{exp} and ±2 mm uncertainty in lengths of individual $T_{185} = 0$ and 1 segments.

At [H_2O] = 1.74 % and $T_{185} = 0.04$ and 0.1, Fig. 2 shows that [O_3] generated using lamp types D and G was approximately 1.7 and 1.8 ppmv; here, lamp type D had one 15 mm quartz segment with $T_{185} = 1$, whereas lamp type G had three 5 mm quartz segments with $T_{185} = 1$. At the same OFR conditions, [O_3] generated using lamp types C and F was 4.5 and 2.7 ppmv; these lamps had one 35 mm and seven 5 mm quartz segments with $T_{185} = 1$. Despite the discrepancy in measured [O_3], corresponding OH_{exp} obtained with lamp types C and F were 2.5×10^{12} and 2.8×10^{12} molec. cm^{-3} s, respectively. Thus, the worse agreement in [O_3] measured between lamp types C and F may be associated specifically with O_3 measurements from these experiments. We hypothesize that the OFR-volume-averaged I_{185} is sufficient to describe associated HO_x production for these cases.

Figure 3 plots OH_{exp} as a function of T_{185} at [H_2O] = 1.90 % ± 0.26 %. The corresponding equivalent photochemical age shown on the right y axis assumes a 24 h average OH concentration of 1.5×10^6 molec cm^{-3} (Mao et al., 2009). Results obtained with lamp types D and G, and C and F were averaged together at $T_{185} = 0.04$ and 0.1, respectively, due to their similar OH_{exp} values. Over the range of T_{185} shown in Fig. 3, excluding lamp type B, OH_{exp} increased by approximately a factor of 5 at $I_{254} = (3.7 \pm 0.6) \times 10^{15}$ photons cm^{-2} s^{-1}) and a factor of 17 at $I_{254} = (2.1 \pm 0.3) \times 10^{14}$ photons cm^{-2} s^{-1}. Maximum OH_{exp} also decreased by about a factor of 5 between lamp types A and B due to reduction in both I_{254} and I_{185} (not shown in Fig. 3). Similar trends were observed for OH_{exp} measurements at [H_2O] = 0.93 % ± 0.06 % and 3.42 % ± 0.30 %, but

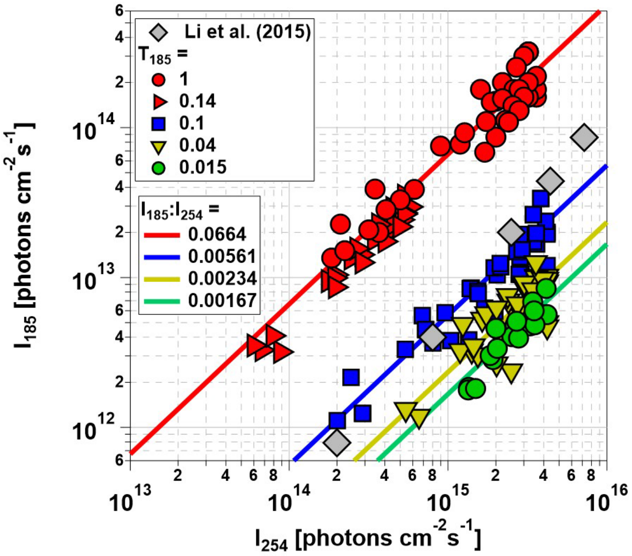

Figure 4. Calculated I_{185} and I_{254} values for the lamp types shown in Fig. 1. I_{185} : I_{254} values were calculated from linear regression functions and used to derive OH_{ex} estimation equations. I_{185} and I_{254} values obtained by Li et al. (2015) in an earlier-generation PAM OFR are shown for reference.

at $[H_2O] = 0.09\,\% \pm 0.07\,\%$, the sensitivity of OH_{exp} to T_{185} was weaker due to suppressed OH production at lower humidity.

3.2 I_{185} : I_{254} determination and derivation of OH_{exp} estimation equations

Figure 4 plots I_{185} as a function of I_{254} for the Hg lamps used in this study and a different model of Hg lamps used in an earlier-generation PAM OFR (Li et al., 2015). As with OH_{exp} values shown in Fig. 3, I_{185} and I_{254} values obtained with lamp types D and G, and C and F were combined together into $T_{185} = 0.04$ and 0.1 symbols following our hypothesis that the OFR-volume-averaged I_{185} was sufficient to describe HO_x production. Linear fits applied to the data shown in Fig. 4 were used to calculate average I_{185} : I_{254} values for lamp types A and B, C and F, D and G, and E. Lamp types A and B (red symbols) had the highest $I_{185} : I_{254} = 0.0664$, whereas lamp type E had the lowest $I_{185} : I_{254} = 0.00167$. $I_{185} : I_{254} = 0.00561$ for lamp types C and F (blue symbols) fell within the envelope of $I_{185} : I_{254} = 0.004$ to 0.012 characterized by Li et al. (2015), with a lower apparent sensitivity of I_{185} : I_{254} to lamp power. This is presumably due to differences in the specific Hg lamp types, potential variability in lamp output within the same lamp type, and/or the method of dimming used in the two studies.

Previous studies reported empirical OH exposure algebraic estimation equations for use with OFRs (Li et al., 2015; Peng et al., 2015, 2018; Lambe et al., 2019). These equations parameterize OH_{exp} as a function of readily measured experimental parameters, therefore providing a simpler alternative than detailed photochemical models for experimental planning and analysis. Here, we expand on those studies by deriving OH_{exp} estimation equations for the lamp types that were used in this study. We adapted the estimation equation format introduced by Li et al. (2015):

$$\log[OH_{exp}] = \Big(a + \big(b + c \times OHR_{ext}^{d} + e \times \log[O_3] \times OHR_{ext}^{f}\big) \times \log[O_3] + \log[H_2O]\Big) + \log\left(\frac{\tau}{124}\right). \quad (1)$$

This equation incorporates the following relationships between OH_{exp} and O_3, H_2O, τ, and OHR_{ext} identified by Li et al. (2015): (1) a power-law dependence of OH_{exp} on UV intensity and, accordingly, $[O_3]$; (2) a linear dependence of OH_{exp} on $[H_2O]$ and τ; (3) OH suppression as a function of increasing OHR_{ext}. The fit coefficients a–f are lamp-specific.

Equation (1) was fit to data obtained from the base case of the model, with CO reacting with OH as a surrogate of OHR_{ext}, over the following OFR185 phase space: $T = 25\,°C$, $\tau = 124\,s$, $OHR_{ext} = 0.77$ to $232\,s^{-1}$, $[H_2O] = 0.1\,\%$ to $3\,\%$, $I_{254} = 10^{13}$ to 10^{16} photons cm^{-2} s^{-1}, and $I_{185} : I_{254} = 0.00167$, 0.00242, 0.00595, and 0.0664. For each I_{185} : I_{254} value, we explored 10, 15, and 20 logarithmically evenly distributed values in the ranges of OHR_{ext}, $[H_2O]$, and I_{254}, respectively. Figure 5 compares OH_{exp} estimated from Eq. (1) and calculated from the model for the $I_{185} : I_{254} = 0.0664$ case. Almost all of the equation-estimated and model OH_{exp} values agreed within a factor or 2 or better. The absolute value of the relative deviations increased above $[H_2O] \approx 0.5\,\%$ and was largest at $[H_2O] = 3\,\%$; the mean absolute value of the relative deviations was 28 %. Analogous plots for $I_{185} : I_{254} = 0.00167$, 0.00242, and 0.00595 cases are shown in Fig. S3 in the Supplement. For these other cases, the mean absolute values of the relative deviations were 20 %, 17 %, and 16 %, respectively. Equation (1) coefficients for lamps with the I_{185} : I_{254} values reported here are presented in Table 2.

To generalize the results shown in Figs. 5 and S3 to OFR185 systems with other I_{185} : I_{254} values, Fig. 6 plots fit coefficients a–f as a function of I_{185} : I_{254}. Each of these coefficients changes monotonically as a function of I_{185} : I_{254}, enabling the usage of simple exponential regression functions to parameterize the a–f values as a continuous function of I_{185} : I_{254}. Exponential function coefficients for the regression curves shown in Fig. 6 are presented in Table 3. Figure 7 compares the equation-estimated OH_{exp} (obtained using Eq. 1 with Table 3 fit coefficients) and the measured OH_{exp} obtained using the tracer decay method. The mean ($\pm 1\sigma$) ratios of equation-estimated and measured OH_{exp} values were 0.94 ± 0.55, 1.13 ± 0.48, 1.03 ± 0.37, and 1.32 ± 0.71 for $I_{185} : I_{254} = 0.00167$, 0.00242, 0.00595, and 0.0664.

Table 2. OH_{exp} estimation equation coefficients ($\pm 1\sigma$) as defined in Eq. (1).

I_{185} : I_{254}	Coefficient					
	a	*b*	*c*	*d*	*e*	*f*
0.00167	16.109 ± 0.321	-0.4734 ± 0.0382	-1.1613 ± 0.0182	0.079284 ± 0.00105	0.99503 ± 0.00195	0.059251 ± 0.00115
0.00242	15.949 ± 0.347	-0.45692 ± 0.0398	-1.0974 ± 0.0186	0.084855 ± 0.0012	0.093976 ± 0.00206	0.064116 ± 0.00134
0.00595	12.306 ± 0.42	-0.070275 ± 0.04130	-0.8052 ± 0.0227	0.11347 ± 0.00249	0.062916 ± 0.00233	0.094896 ± 0.00291
0.0664	10.098 ± 0.576	0.15062 ± 0.0455	-0.44244 ± 0.0329	0.18041 ± 0.00872	0.031146 ± 0.00265	0.1672 ± 0.00953

Table 3. Parameterization of Eq. (1) coefficients ($\pm 1\sigma$): $y0 + A \times \exp[I_{185} : I_{254}) \times \mathrm{invTau}]$.

Coefficient	y0	A	invTau
a	10.053 ± 0.593	9.4455 ± 1.52	230.41 ± 71.8
b	0.15553 ± 0.0641	-0.99468 ± 0.168	237.54 ± 76.9
c	0.44174 ± 0.0106	-0.95747 ± 0.0223	163.04 ± 8.41
d	0.18069 ± 0.000904	-0.12054 ± 0.00161	98.577 ± 3.91
e	0.031037 ± 0.00208	0.094968 ± 0.00462	182.31 ± 18.8
f	0.16754 ± 0.00167	-0.1287 ± 0.00295	96.245 ± 6.65

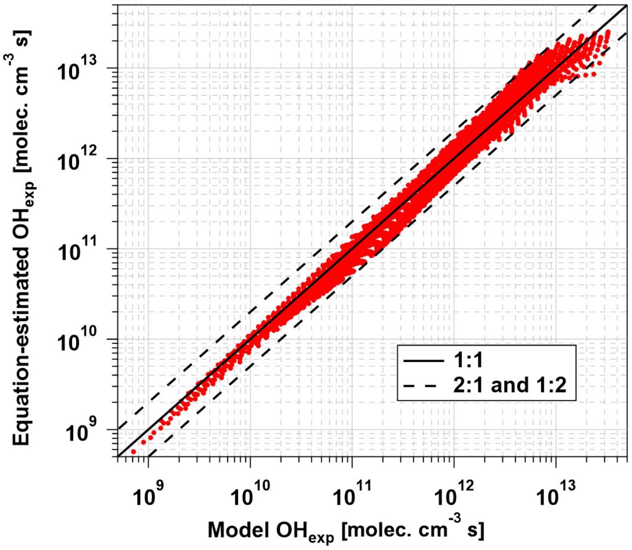

Figure 5. OH_{exp} calculated from the estimation equation (Eq. 1) as a function of OH_{exp} calculated from the full OFR185 KinSim mechanism (Table S1) for lamp types A and B. Solid and dashed lines correspond to the 1 : 1 and the 1 : 2 and 2 : 1 lines, respectively. Estimation equation fit coefficients are shown in Table 2.

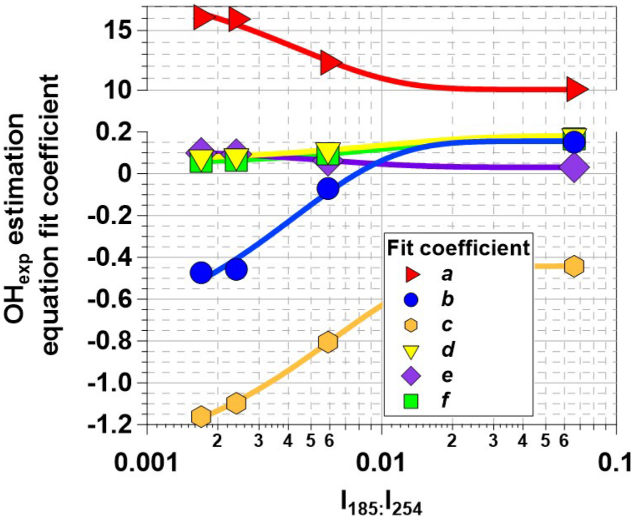

Figure 6. OH_{exp} estimation equation fit coefficients plotted as a function I_{254} : I_{254}. Trend lines were calculated from exponential regression functions with fit parameters that are presented in Table 3.

3.3 Influence of I_{185} on HO_2, NO_x, and UV photolysis of aromatic volatile organic compounds

[HO_2] and [NO_x] (with N_2O present) increase along with [OH] as a function of I_{185} (Fig. S4 in the Supplement). To isolate the effect of I_{185} on related OFR photochemistry at fixed OH_{exp}, we investigated two OFR185 cases using (I_{185}, I_{254}) = (3.33×10^{12}, 1.96×10^{15}) and (6.65×10^{12}, 1.01×10^{14}) photons $cm^{-2}\,s^{-1}$ that each generate a model-calculated $OH_{exp} = 5.0 \times 10^{11}$ molec. cm^{-3} s at base-case conditions of [H_2O] = 2 %, $\tau = 124$ s, and $OHR_{ext} = 30\,s^{-1}$. These cases were designated as "low" and "high" I_{185} : I_{254} cases. Thus, increasing I_{185} by a factor of 2 enabled lowering I_{254} by a factor of 20 to achieve equivalent OH_{exp}.

First, we investigated the resilience of each OFR185 case to OH suppression via OHR_{ext}. As OHR_{ext} was increased from 30 to 300 s^{-1}, OH_{exp} decreased from 5.0×10^{11} to 7.9×10^{10} (low I_{185} : I_{254}) and 9.0×10^{10} (high I_{185} : I_{254}) molec. $cm^{-3}\,s^{1}$. Thus, increasing I_{185} decreased OH

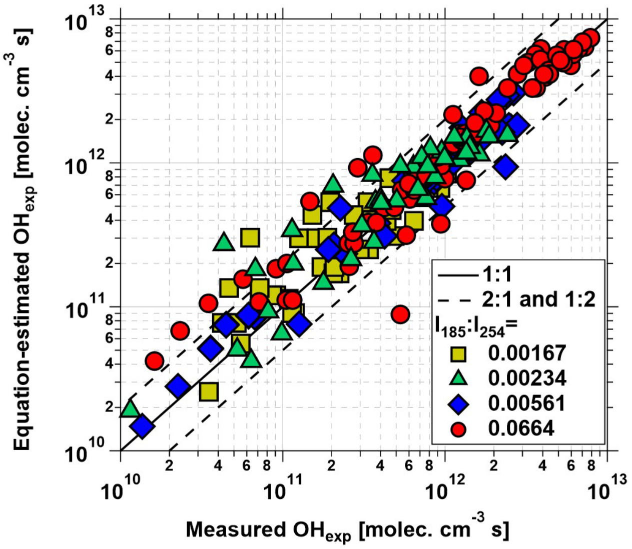

Figure 7. OH_{exp} calculated from estimation equation (Eq. 1 and Table 2) as a function of OH_{exp} calculated from tracer decay method for Hg lamp types with $I_{254}:I_{254}$ values specified in the legend.

suppression by 15 %, primarily due to 30 % higher $[HO_2]$ in the high $I_{185}:I_{254}$ case that increased the $OH+HO_2$ reaction rate and partially buffered the system against increasing OHR_{ext}. Second, we compared the ability of each OFR185 case to generate high-NO conditions in the presence of added $[N_2O]$. For example, at $[N_2O] = 2.7\,\%$, $NO : HO_2 = 1$ and 0.4 at low and high $I_{185}:I_{254}$. While increasing $[N_2O]$ from 2.7 % to 4.0 % achieved $NO : HO_2 = 1$ at high $I_{185}:I_{254}$, $[NO_2]$ also increased from 50 to 100 ppbv. At higher UV intensity, a similar increase in $[N_2O]$ could generate $[NO_2] > 1$ ppm and promote artificially fast $RO_2 + NO_2$ reactions compared to atmospheric conditions (Peng and Jimenez, 2017). Third, we compared relative timescales for OH oxidation and photolysis of representative aromatic volatile organic compounds (VOCs) that absorb $\lambda = 185$ and 254 nm radiation. The fractional VOC loss due to photolysis, $F_{\text{photolysis}}$, was calculated using Eq. (2):

$$F_{\text{photolysis}} = \frac{\sigma_{185} I_{185} \phi_{185} + \sigma_{254} I_{254} \phi_{254}}{\sigma_{185} I_{185} \phi_{185} + \sigma_{254} I_{254} \phi_{254} + k_{\text{OH}}[\text{OH}]}, \qquad (2)$$

where σ_{185} and σ_{254} are the VOC absorption cross sections at $\lambda = 185$ and 254 nm, ϕ_{185} and ϕ_{254} are the VOC photolysis quantum yields, and k_{OH} is the bimolecular reaction rate coefficient with OH. Assuming upper limit $\phi_{185} = 1$ and $\phi_{254} = 1$ values, $\sigma_{185} = 2.8 \times 10^{-17}\,\text{cm}^2$, $\sigma_{254} = 8.9 \times 10^{-19}\,\text{cm}^2$ (Dawes et al., 2017), and $k_{OH} = 1.28 \times 10^{-12}\,\text{cm}^3\,\text{molec}^{-1}\,\text{s}^{-1}$ (Atkinson, 1986), $F_{\text{photolysis, benzene}} \leq 0.26$ and 0.07 at low and high $I_{185}:I_{254}$. Similarly, $F_{\text{photolysis, toluene}} \leq 0.07$ and 0.04 at low and high $I_{185}:I_{254}$ (Atkinson, 1986; Serralheiro et al., 2015).

4 Conclusions

OFR185 is emerging as one of the most commonly used OFR methods by enabling efficient HO_x and NO_x generation over a range of oxidative aging timescales that are relevant to atmospheric processes. Important OFR185 parameters are I_{185}, I_{254}, $[H_2O]$, $[N_2O]$ (if NO_x generation is required), OHR_{ext}, and τ_{OFR}. However, $I_{185}:I_{254}$ is specific to the Hg lamp and/or OFR, as are associated calibration and estimation equations. To develop a general framework within which to evaluate and compare different OFR185 systems, we characterized OH_{exp} as a function of I_{185}, I_{254}, OHR_{ext}, and $[H_2O]$ values, in the process using several novel low-pressure Hg lamp configurations to extend the range of achievable $I_{185}:I_{254}$. OH_{exp} estimation equations were developed for the Hg lamp types that were used, and corresponding estimation equation fit coefficients were parameterized as a function of $I_{185}:I_{254}$ to enable interpolation to other OFR185 systems that can employ the same Hg lamp type(s) over the range of $[O_3]$, $[H_2O]$, OHR_{ext}, and τ values parameterized here. Because low-pressure Hg germicidal fluorescent lamps are used in many industries (e.g., medical, HVAC, wastewater remediation), they are less expensive and more easily acquired than other Hg lamps. OHR_{int}, HO_2:OH, and $F_{photolysis}$ were improved at higher $I_{185}:I_{254}$, whereas $NO : HO_2$ and $NO : NO_2$ were improved at lower $I_{185}:I_{254}$. Overall, our results suggest that optimal OFR185 performance is achieved by (1) maximizing $I_{185}:I_{254}$, (2) reducing OH_{exp} (if needed) through simultaneous reduction in I_{185} and I_{254} via electronically or mechanically dimming the lamp output (Fig. S2), and (3) increasing $[N_2O]$ to offset higher $[HO_2]$ if high-NO conditions are required, provided that $[NO_2]$ does not exceed ≈ 1 ppm, in which case lower $I_{185}:I_{254}$ should be used. Future work will investigate the sensitivity of NO_x-dependent, OH-initiated oxygenated volatile organic compound and SOA formation processes to $I_{185}:I_{254}$.

Code and data availability. Data presented in this paper are available upon request. The KinSim mechanism can be downloaded from the Supplement. The kinetic solver is freely available at https://tinyurl.com/kinsim-cases#bookmark=kix.6zu8zdwq2lce. (Peng and Jimenez, 2020b).

Supplement. The supplement related to this article is available online at: https://doi.org/10.5194/acp-20-13417-2020-supplement.

Author contributions. AL conceived and planned the experiments. JR performed the experiments. JR and AL performed the data analysis. JR, AL, and WB conceived and planned the model simulations, and JR and AL carried out the model simulations. JR, AL, and WB contributed to the interpretation of the results. AL took the lead in writing the paper. All authors provided feedback on the paper.

Competing interests. The authors declare that they have no conflict of interest.

Acknowledgements. We thank Chris Rockett (Light Sources Inc.), Dan Spicer (Light Sources Inc.), Leah Williams (Aerodyne), and John Jayne (Aerodyne) for helpful discussions.

Review statement. This paper was edited by Eliza Harris and reviewed by two anonymous referees.

References

Atkinson, R.: Kinetics and mechanisms of the gas-phase reactions of the hydroxyl radical with organic compounds under atmospheric conditions, Chem. Rev., 86, 69–201, 1986.

Dawes, A., Pascual, N., Hoffmann, S. V., Jones, N. C., and Mason, N. J.: Vacuum ultraviolet photoabsorption spectroscopy of crystalline and amorphous benzene, Phys. Chem. Chem. Phys., 19, 27544–27555, https://doi.org/10.1039/C7CP05319C, 2017.

Huang, Y., Coggon, M. M., Zhao, R., Lignell, H., Bauer, M. U., Flagan, R. C., and Seinfeld, J. H.: The Caltech Photooxidation Flow Tube reactor: design, fluid dynamics and characterization, Atmos. Meas. Tech., 10, 839–867, https://doi.org/10.5194/amt-10-839-2017, 2017.

Lambe, A. T., Ahern, A. T., Williams, L. R., Slowik, J. G., Wong, J. P. S., Abbatt, J. P. D., Brune, W. H., Ng, N. L., Wright, J. P., Croasdale, D. R., Worsnop, D. R., Davidovits, P., and Onasch, T. B.: Characterization of aerosol photooxidation flow reactors: heterogeneous oxidation, secondary organic aerosol formation and cloud condensation nuclei activity measurements, Atmos. Meas. Tech., 4, 445–461, https://doi.org/10.5194/amt-4-445-2011, 2011.

Lambe, A. T., Krechmer, J. E., Peng, Z., Casar, J. R., Carrasquillo, A. J., Raff, J. D., Jimenez, J. L., and Worsnop, D. R.: HO_x and NO_x production in oxidation flow reactors via photolysis of isopropyl nitrite, isopropyl nitrite-d_7, and 1,3-propyl dinitrite at $\lambda = 254$, 350, and 369 nm, Atmos. Meas. Tech., 12, 299–311, https://doi.org/10.5194/amt-12-299-2019, 2019.

Li, R., Palm, B. B., Ortega, A. M., Hlywiak, J., Hu, W., Peng, Z., Day, D. A., Knote, C., Brune, W. H., De Gouw, J. A., and Jimenez, J. L.: Modeling the Radical Chemistry in an Oxidation Flow Reactor: Radical Formation and Recycling, Sensitivities, and the OH Exposure Estimation Equation, J. Phys. Chem. A, 119, 4418–4432, 2015.

Mao, J., Ren, X., Brune, W. H., Olson, J. R., Crawford, J. H., Fried, A., Huey, L. G., Cohen, R. C., Heikes, B., Singh, H. B., Blake, D. R., Sachse, G. W., Diskin, G. S., Hall, S. R., and Shetter, R. E.: Airborne measurement of OH reactivity during INTEX-B, Atmos. Chem. Phys., 9, 163–173, https://doi.org/10.5194/acp-9-163-2009, 2009.

Peng, Z. and Jimenez, J. L.: Modeling of the chemistry in oxidation flow reactors with high initial NO, Atmos. Chem. Phys., 17, 11991–12010, https://doi.org/10.5194/acp-17-11991-2017, 2017.

Peng, Z. and Jimenez, J. L.: KinSim: A Research-Grade, User-Friendly, Visual Kinetics Simulator for Chemical-Kinetics and Environmental-Chemistry Teaching, J. Chem. Educ., 96, 806–811, https://doi.org/10.1021/acs.jchemed.9b00033, 2019.

Peng, Z. and Jimenez, J. L.: Radical chemistry in oxidation flow reactors for atmospheric chemistry research, Chem. Soc. Rev., 49, 2570–2616, https://doi.org/10.1039/C9CS00766K, 2020a.

Peng, Z. and Jimenez, J.: Downloadable KinSim cases and mechanisms, available at: https://tinyurl.com/kinsim-cases#bookmark=kix.6zu8zdwq2lce, last access: 15 May 2020b.

Peng, Z., Day, D. A., Stark, H., Li, R., Lee-Taylor, J., Palm, B. B., Brune, W. H., and Jimenez, J. L.: HO_x radical chemistry in oxidation flow reactors with low-pressure mercury lamps systematically examined by modeling, Atmos. Meas. Tech., 8, 4863–4890, https://doi.org/10.5194/amt-8-4863-2015, 2015.

Peng, Z., Day, D. A., Ortega, A. M., Palm, B. B., Hu, W., Stark, H., Li, R., Tsigaridis, K., Brune, W. H., and Jimenez, J. L.: Non-OH chemistry in oxidation flow reactors for the study of atmospheric chemistry systematically examined by modeling, Atmos. Chem. Phys., 16, 4283–4305, https://doi.org/10.5194/acp-16-4283-2016, 2016.

Peng, Z., Palm, B. B., Day, D. A., Talukdar, R. K., Hu, W., Lambe, A. T., Brune, W. H., and Jimenez, J. L.: Model Evaluation of New Techniques for Maintaining High-NO Conditions in Oxidation Flow Reactors for the Study of OH-Initiated Atmospheric Chemistry, ACS Earth Space Chem., 2, 72–86, https://doi.org/10.1021/acsearthspacechem.7b00070, 2018.

Peng, Z., Lee-Taylor, J., Orlando, J. J., Tyndall, G. S., and Jimenez, J. L.: Organic peroxy radical chemistry in oxidation flow reactors and environmental chambers and their atmospheric relevance, Atmos. Chem. Phys., 19, 813–834, https://doi.org/10.5194/acp-19-813-2019, 2019.

Serralheiro, C., Duflot, D., da Silva, F. F., Hoffmann, S. V., Jones, N. C., Mason, N. J., Mendes, B., and Limão-Vieira, P.: Toluene Valence and Rydberg Excitations as Studied by ab initio Calculations and Vacuum Ultraviolet (VUV) Synchrotron Radiation, J. Phys. Chem. A, 119, 9059–9069, https://doi.org/10.1021/acs.jpca.5b05080, 2015.

Spicer, D.: Germicidal Lamp Basics, available at: https://www.light-sources.com/wp-content/uploads/2015/05/Germicidal_Lamp_Basics_-_2013.pdf (last access: 23 April 2020), 2013.